RESEARCH ARTICLE

ADVANCED OPTICAL MATERIALS
www.advopticalmat.de

Tunable-Wavelength Broadband Liquid-State Carbon-Quantum-Dot Lasers

*Xuezhe Dong, Pengzhi Wang, Wei Gao, Ting Wang, Luwei Zhou, Chen Yang, Shaofeng Zhang, Yimin Jiang, Mingjie Li, and Siu Fung Yu**

Stimuli-responsive carbon quantum dots (CQDs) are versatile, solution-processable, liquid-state gain media with broadband spectral tunability spanning ultraviolet to near-infrared wavelengths, attributed to their surface functionalization capabilities and environmental sensitivity. However, their application in high-coherence light sources is constrained by inherent scattering losses and lower gain coefficients relative to conventional colloidal quantum dots. To address these limitations, concentration-dependent photoluminescent are engineered CQDs integrated into an index-matched cuvette-based cavity, enabling tunable liquid-state lasing across the 641–710 nm spectral range via the Förster resonance energy transfer (FRET) effect. The FRET-optimized CQDs exhibit minimized beam divergence emission, facilitating efficient coupling with an external optical cavity—comprising an aluminum mirror positioned outside the cuvette-based cavity. By modulating the external optical feedback, controlled transitions from random lasing to Fabry–Pérot multimode, and single-mode lasing regimes are achieved. Notably, this design methodology is applicable to colloidal quantum dots as liquid-state gain media, establishing a versatile platform for spectrally tunable lasing sources. This work bridges the gap between solution-processable nanomaterials and functional laser devices, advancing prospects for integrated photonic systems.

1. Introduction

Owing to their low cost and ease of synthesis, carbon quantum dots (CQDs) have garnered significant attention as promising solution-processable candidates for next-generation light sources, including light-emitting devices and lasers.[1–4] A defining feature of CQDs is their tunable energy levels, which stem from surface reactivity and diverse functional groups (e.g., carboxyl, amine, and epoxy groups).[5–8] This tunability enables CQDs to emit light across a broad spectrum, spanning ultraviolet to near-infrared regions—a capability that surpasses many conventional nanomaterials.[9,10] Consequently, CQDs are considered a potential candidate for realizing wide-bandwidth tunable lasing devices.[11–13] Compact CQD-based lasers can commonly be realized using quartz cuvettes filled with CQDs uniformly dispersed in a solvent as a liquid gain medium.[14,15] However, achieving multi-wavelength lasing requires precise integration of mirrors directly onto quartz surfaces alongside controlled beam collimation, often necessitating external mounts that introduce alignment instability.[16,17] These complexities complicate the fabrication of tunable CQD lasers. A further challenge arises from weak light scattering caused by Rayleigh scattering in the solvent dispersed with CQDs, which reduces the optical gain of CQDs.[18–20] Achieving compact, low-cost, and wavelength-tunable CQDs lasers requires a thorough understanding and precise control of lasing physics in liquid gain media—a significant challenge in current research.[21] Key obstacles include overcoming limitations in optical confinement, ensuring precision in component alignment, and seamlessly integrating external components with the liquid-filled cuvette.

In this study, we introduce an innovative gain-guided waveguide framework for cuvette-based color-tunable carbon quantum dots (TCQDs) as a laser cavity.[22–24] By leveraging the aggregation-induced Förster resonance energy transfer (FRET) effect, we achieve spontaneous emission across a broad wavelength range (587–710 nm). This approach simultaneously enables light confinement within the cavity and external collimation of propagating light, facilitated by a solvent whose refractive

X. Dong, P. Wang, W. Gao, T. Wang, L. Zhou, C. Yang, S. Zhang, Y. Jiang, M. Li, S. F. Yu
Department of Applied Physics
The Hong Kong Polytechnic University
Hung Hom, Hong Kong, Kowloon 999077, China
E-mail: apsfyu@polyu.edu.hk
X. Dong, P. Wang, W. Gao, T. Wang, L. Zhou, C. Yang, S. Zhang, Y. Jiang, M. Li, S. F. Yu
Shenzhen Research Institute
The Hong Kong Polytechnic University
Shenzhen, Guangdong 518057, China

The ORCID identification number(s) for the author(s) of this article can be found under https://doi.org/10.1002/adom.202500737

DOI: 10.1002/adom.202500737

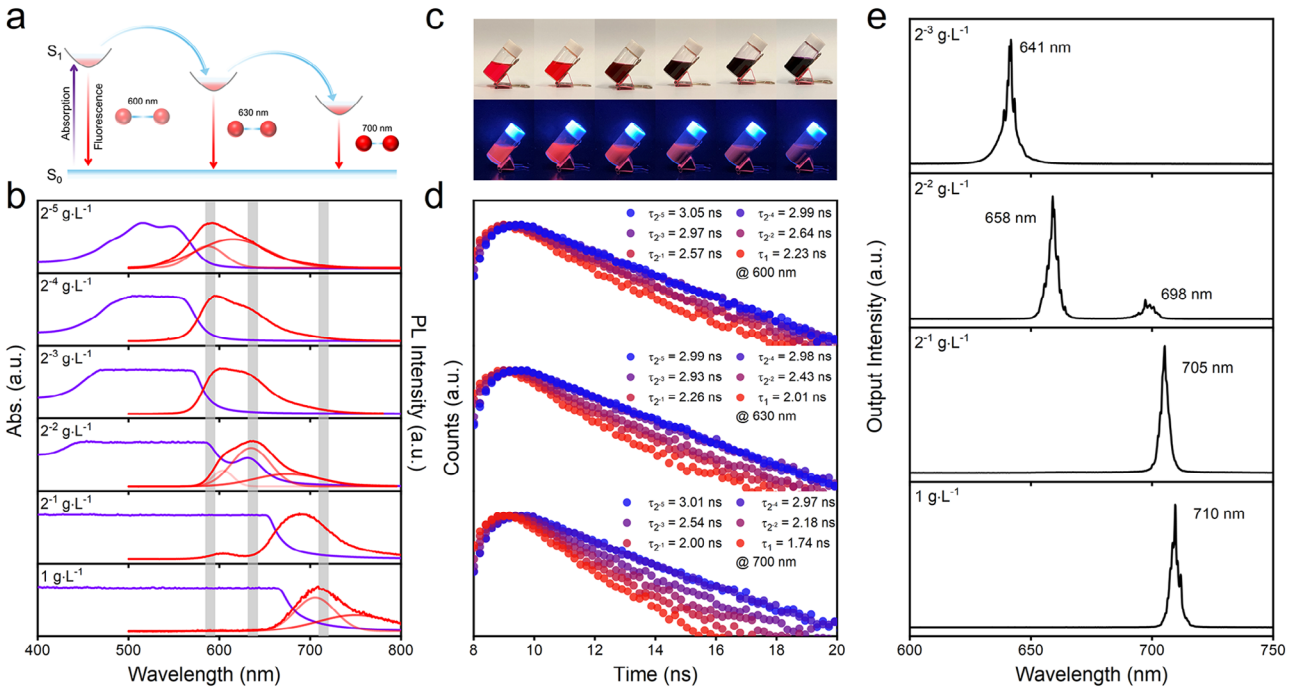

Figure 1. a) Schematic of the concentration-dependent FRET process within multi-level systems. b) Concentration-dependent optimal PL spectra and absorption spectra from 2^{-5} g·L^{-1} to 1 g·L^{-1} in DMF. c) Photos of different concentration TCQDs under sunlight (top) and UV lamp (bottom). d) Concentration-dependent TRPL spectra at 600, 630, and 700 nm. e) Tunable multiband lasing due to FRET. From bottom to top, the corresponding concentration is 2^{-3} g·L^{-1}, 2^{-2} g·L^{-1}, 2^{-1} g·L^{-1}, 1 g·L^{-1}.

index matches that of the cuvette. This refractive index matching enhances coupling efficiency between the output laser and the external cavity. By integrating the cuvette with an external flat aluminum mirror, we demonstrate that strong optical feedback coupling drives a critical transition from random lasing to controlled Fabry–Pérot multimode and single-mode lasing regimes. This advancement in lasing device design enables the fabrication of low-cost, compact CQDs lasers with programmable modal control, enhancing precision and adaptability for photonic systems applications. Hence, we delineate a pathway to achieving precise control over lasing properties, thereby paving the way for future developments in wavelength-tunable photonic systems. This study not only contributes to the growing body of knowledge on CQDs but also sets the stage for the next generation of adaptable, high-performance photonic devices.

2. Results and Discussion

2.1. FRET-Induced Fluorescent Color Shift and Multiband Lasing

A class of size-homogeneous, monodisperse, *O*-phenylenediamine-based TCQDs was synthesized by a solvothermal method to serve as the liquid-state gain medium (see Experimental Section for details). Transmission electron microscopy (TEM) and high-resolution TEM (HRTEM) images (see Figure S1, Supporting Information) confirmed the uniform spherical morphology of the TCQDs, with an average lateral size of 4 nm and a well-defined lattice spacing of 0.21 nm, corresponding to the (100) plane of graphene. Steady-state photoluminescence (PL) and absorption spectra at concentrations ranging from 2^{-5} g·L^{-1} to 1 g·L^{-1} were analyzed to elucidate the energy transfer process, see **Figure** 1a,b. The modification of the energy transfer pathway was confirmed by the emergence of new absorption peaks at 630 nm at 2^{-3} g·L^{-1}, compared to the peaks at 480, 515, and 545 nm dominated at lower concentrations. The TCQDs demonstrated aggregation-induced redshifted radiative channels, with emission spanning from 585 nm at concentrations of 2^{-5} g·L^{-1} to 700 nm at 1 g·L^{-1}. These emissions were deconvoluted into 3 stable luminescent centers at ≈600, ≈630, and ≈700 nm) under varying excitation wavelengths (see Figure S2, Supporting Information), verified by a visible color transition from bright orange to deep red under UV illumination, see Figure 1c. Concentration-dependent shifts in PL excitation peaks (see Figure S3, Supporting Information) further revealed excited-state transitions. A progressive blue shift in the short-wavelength excitation peak (2^{-5} g·L^{-1}, 520 nm) and a concomitant red shift in the long-wavelength excitation peak (2^{-5} g·L^{-1}, 612 nm) competitively emerged, aligning with the evolution of absorption spectra. The increasing overlap between PL and absorption spectra confirmed FRET.[25]

Time-resolved photoluminescence (TRPL) decay trends, see Figure 1d, provided robust evidence of the FRET effect. The observed decrease in fluorescence lifetime (3.05 ns to 2.23 ns at 600 nm, 2.99 to 2.01 ns at 630 nm, 3.01 ns to 1.74 ns at 700 nm) followed with a gradual increase of the concentration of TCQDs indicated that the FRET phenomenon effectively enhanced the probability of photon population at lower energy levels.[26] The coefficient of FRET, calculated as $\eta_{FRET} = 1 - (\tau_{DA}/\tau_D)$ (where τ_{DA} and τ_D are lifetimes with and without the acceptor,

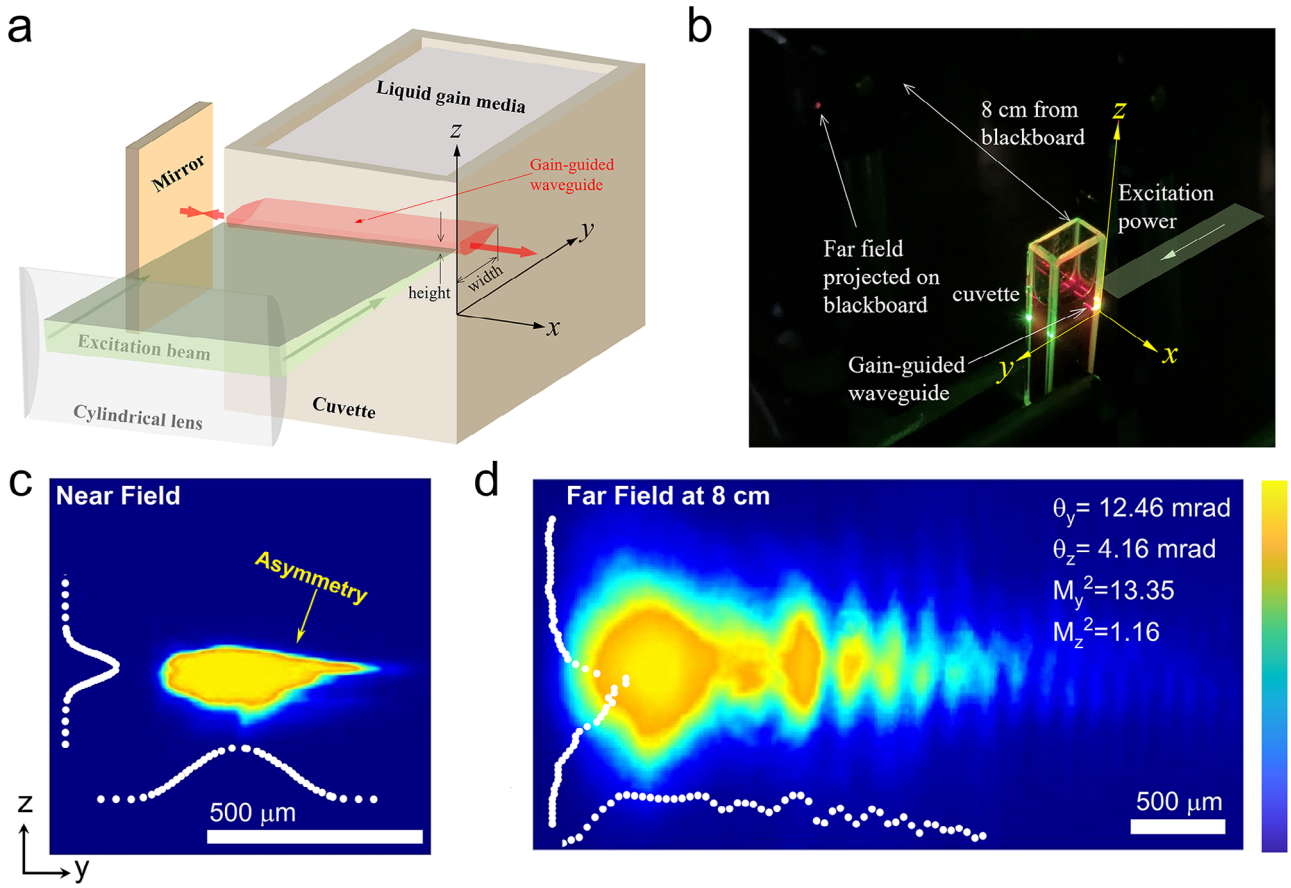

Figure 2. a) Schematic diagram of gain-guided waveguide based on cuvette filled with TCQDs solutions. b) Photo – experimental setup for the measurement of the far-field laser beam emitted from the TCQDs-filled cuvette without an external mirror. c) Near-field beam profile. d) Far-field beam profile captured at a distance of 8 cm from the cuvette. Inset curves are measured profiles in the y and z direction.

respectively), increased significantly (see Figure S4, Supporting Information) as the 630 nm absorption peak intensified at 2^{-3} g·L^{-1}, confirming efficient photon redistribution to lower energy states. This analysis highlights the critical role of concentration-dependent carrier dynamics in optimizing luminescent properties, providing key insights for designing advanced photonic materials.

An intriguing phenomenon was observed when the concentration of TCQDs was halved progressively, resulting in a blue shift of the laser peak from 710 to 641 nm (Figure S5, Supporting Information). Significantly, the emission spectra exhibited random lasing characteristics, with the lasing threshold increasing from 1.91 to 27.85 mJ·cm^{-2} as the TCQD concentration was reduced from 2–3 g·L^{-1} to 1 g·L^{-1}. At low concentrations near the lasing threshold, the emission spectrum exhibits a single lasing spike. As excitation power increases, additional spikes emerge, suggesting that the liquid medium functions as a weakly scattering random system with coherent optical feedback, indicative of closed-loop cavity formation within the medium. At higher concentrations and excitation powers exceeding the threshold, multiple spikes emerge and merge due to spectral overlap, a phenomenon attributed to the increased density of overlapping closed-loop cavities in high-concentration solutions. Fourier transform analysis of the laser emission spectra further reveals that the cavity lengths associated with these random modes are below 100 μm and decrease with increasing concentration, aligning with the principle that higher scattering medium concentrations reduce lasing thresholds. On the other hand, when the gain medium concentration was further reduced to 2^{-4} g·L^{-1}, population inversion could not be sustained at wavelengths near 600 and 630 nm (Figure S6, Supporting Information).

2.2. Explanation of the Formation of Gain-Guided Waveguide

Figure 2a illustrates the design of the CQD laser with external optical feedback. The quartz cuvette is filled with a solvent containing uniformly dispersed CQDs. The solvent's refractive index is selected to closely match that of the quartz cuvette, thereby preventing the formation of an index-guided structure. To create a gain-guided waveguide within the cuvette, a cylindrical lens focuses the 532 nm excitation beam into a line along the cuvette's length (*x*-axis), as depicted in Figure 2a. The resulting emission (600–700 nm) is confined along the z-direction due to a gain difference between excited and unexcited regions. Simultaneously, the excitation light penetrates the solvent, providing gain confinement along the *y*-axis with a penetration depth <500 μm. This configuration achieves 2D light confinement

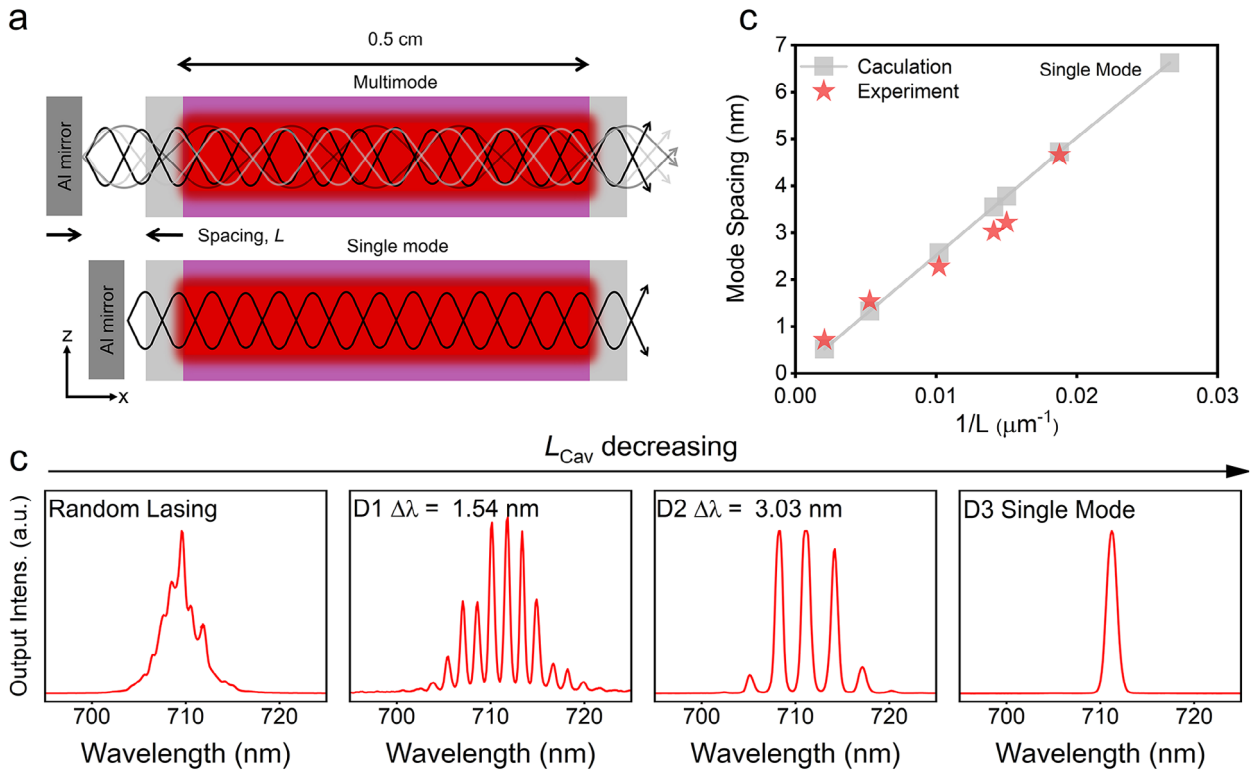

Figure 3. a) Schematic diagram of a TCQD solution-filled quartz cuvette with an external Al mirror (left-hand side). b) Lasing spectra versus different spacings, *L*. As the air gap spacing, *L*, between the mirror and cuvette decreases, the lasing mode transitions sequentially from the random lasing regime to Fabry–Pérot multi-mode lasing and ultimately to single-mode lasing. c) The linear relationship between mode spacing $\Delta\lambda$ and L^{-1} (reciprocal of *L*) of TCQDs solution.

(*z*- and *y*-directions), forming a gain-guided waveguide (red channel in Figure 2a). The waveguide dimensions are ≈200 μm in height (*z*-axis) and <500 μm in width (*y*-axis), while light propagates freely along the *x*-axis. Optical feedback is established through an external mirror, forming a coupled cavity with the cuvette. The coupled cavity and the air-cuvette interfaces on the opposing sides of the quartz cuvette define the resonant cavity for the gain-guided laser system. The optical gain coefficient and cavity loss of TCQD solutions (1 g·L^{-1} in DMF) were quantified using the VSL and VCL methods (see Experimental Section). The measured optical gain of 5.85 cm^{-1} exceeds the cavity loss of 4.773 cm^{-1} under an incident pump fluence of 1.217 mJ·cm^{-2}. At higher excitation power, the gain coefficient increases linearly to 50.17 cm^{-1}, representing the highest value recorded for carbon dots (Figure S7, Supporting Information). This confirms that the design of CQDs cavity is capable of supporting lasing emission.

Figure 2c–d show the near- and far-field profiles, respectively, measured using a spot analyzer from the cuvette, as captured by the setup illustrated in Figure 2b. The near-field emission beam exhibits a "water droplet" spatial profile with an extended tail along the *y*-axis, measuring ≈488 μm in width and ≈254 μm in height along the *z*-axis. This droplet-shaped emission arises from the spatially non-uniform excitation profile of the 532 nm pump light along the *y*-axis (see Figure 2a). Due to absorption in the liquid gain medium, the pump intensity decays exponentially with penetration distance, resulting in stronger light generation near the cuvette edge (smaller *y*) and diminished emission at larger *y*, thereby forming the observed droplet profile. The current excitation geometry—using a cylindrical lens to focus the pump beam into a line on the liquid gain medium—inherently produces this asymmetric near-field emission. To mitigate the elongated tail of the droplet profile, a viable strategy involves reducing the excitation beam's thickness by narrowing its transverse width along the *z*-axis. This adjustment would spatially confine the excitation region, flatten the intensity gradient along the y-direction, and yield a more uniform emission profile. The near-field droplet-shaped profile adversely impacts far-field beam quality (Figure 2d), producing a meteor-shaped far-field beam with $1/e^2$ intensity half-widths of 847.5 and 342.5 μm. The calculated divergence angles of θ_y = 12.46 mrad and θ_z = 4.16 mrad confirm low-beam divergence over a long-distance propagation. Therefore, the far-field profile projected onto a blackboard 8 cm from the cuvette (Figure 2b) demonstrates a collimated beam, verifying that the gain-guided waveguide provides strong light confinement within the cuvette and maintains collimation outside, making it suitable for use as a laser cavity.

2.3. Programmable Mode-Spacing Liquid Laser Based on External Mirror

Figure 3a (see also Figure 2a; Figure S5, Supporting Information) illustrates how external optical feedback tailors the laser mode from random lasing to Fabry–Pérot lasing by adjusting

the spacing, L, between an aluminum mirror and one side of the quartz cuvette-filled with TCQD solution (1 g·L^{-1} in DMF). Figure 3b demonstrates the emission spectral changes of the cuvette without and with optical feedback via the external Al mirror (see also Figure S8 and Video S1, Supporting Information). While the cuvette inherently supports random lasing, the introduction of the external Al mirror modifies the modal characteristics to Fabry-Pérot modes, arising from the coupled external cavity. Furthermore, the mode spacing $\Delta\lambda$ increases as L decreases. The linear relationship between L^{-1} (the reciprocal of L) and $\Delta\lambda$ is shown in Figure 3c. As L decreases from 485.23 µm to 53.28 µm, $\Delta\lambda$ increases from ≈0.71 to ≈4.66 nm, with single-mode lasing achieved at L ≈38.04 µm. The measured $\Delta\lambda$ and L are fitted to the Fabry–Pérot cavity model: $\Delta\lambda = \lambda^2/(2n_{\text{eff}}L)$ where λ is the lasing wavelength and n_{eff} (effective refractive index of the coupled external cavity) is found to be 1.00029. The proximity of n_{eff} to the refractive index of air confirms that the air gap between the Al mirror and cuvette (i.e., external cavity) defines the Fabry–Pérot modes, independent of the cuvette's physical cavity length (0.5 cm). The measured cavity loss of the liquid gain medium (4.773 cm^{-1}) corresponds to a penetration length of 0.2 cm, which value is compatible with the cuvette's cavity length. Consequently, the strong optical feedback with Fabry–Pérot modal characteristics suppresses closed-loop cavities (cavity length < 100 µm). Furthermore, the refractive index match between the solvent and quartz cuvette prevents constructive or destructive interference of the feedback light, enabling the Fabry-Pérot modes from the coupled external cavity to propagate and emit from the cuvette. A further advantage of strong optical feedback is the enhancement of the Q-factor in CQD lasers. As shown in Figure 3b, the introduction of an aluminum mirror reduces the lasing linewidth from ≈6 nm (random lasing) to ≈2 nm (single-mode lasing), resulting in a threefold improvement in the Q-factor.

We examined the impact of refractive index on phase coherence using four types of solvents, with effective refractive indices of 1.499 for DMSO, 1.450 for DMF, 1.38 for ethanol, and 1.37 for acetone. Surprisingly, lasing was observed only in DMSO and DMF, where refractive indices matched or slightly exceeded that of the quartz cuvette wall. Similar to DMF, TCQDs in DMSO also exhibited mode spacing modulation (Figure S9, Supporting Information). The refractive index critically influenced the laser performance, as indicated by the larger number of spikes observed in DMF compared to DMSO (Figure S10a, Supporting Information). In contrast, only spontaneous emission was detected in ethanol and acetone, which have lower refractive indices. To gain deeper insights into these observations, we conducted simulations of the electric field distribution using two different refractive indices to investigate why higher refractive indices enhance laser performance (Figure S10b, Supporting Information). In environments with low refractive indices, standing waves struggle to localize and accumulate in the desired direction. Conversely, in solutions with higher refractive indices, the emitted light was effectively confined within the spacer formed by the cuvette walls. These simulations revealed that coherence diminishes when light interacts with materials that have refractive indices significantly lower than that of quartz. In experiments with higher refractive indices, intense interference was observed, facilitating light propagation in the desired direction along the active region. This understanding underscores the critical role of refractive index in optimizing laser performance.

2.4. Transient State Absorption of TCQDs Solution

Due to the low transmittance of high-concentration solutions, transient absorption (TA) spectra of 2^{-2} g·L^{-1} were selected to study carrier dynamics under varying incident power densities (1.19 to 3.58 J•cm^{-2}, Figure S11, Supporting Information). Two distinct opposing signals are observed in the TA spectra (**Figure 4a**). The negative region before 570 nm is attributed to ground-state bleaching (GSB), consistent with the steady-state UV–vis absorption spectra. TA spectra at different delay times within a timescale of 5 ns explored the carrier dynamics in depth. The first process, occurring within 1.09 ps, illustrated the dynamics, where absorption peaks at 515 and 550 nm appeared and gradually increased as the delay time progressed. Meanwhile, the peak attributed to excited state absorption (ESA) at 600 nm continued rising, corresponding to significant absorption loss in the excited state, which is detrimental to population inversion. The second process occurred within a delay time range of 1.61–6.14 ps. The initial two peaks at 515 and 550 nm gradually decreased with a slight blue shift, while the peak at 470 nm continued to grow, consistent with the photoluminescence excitation (PLE) spectra. As the delay time increased further, the absolute values of all peaks significantly decreased, except for GSB at 450 nm.

The observations suggest that pump light excitation rapidly induces two distinct transition pathways, generating photogenerated carriers that populate absorption bands at 515 and 550 nm, with dominant photon emission at 600 nm. Ground state bleaching (GSB) at 515 nm emerged as the dominant signal immediately following initial excitation. Subsequently, after 6.14 ps, the higher energy level at 470 nm began to play a more prominent role, leading to the emission of longer-wavelength photons. This photo-excitation process indicates that energy levels corresponding to wavelengths above 630 nm achieved population inversion (Figure S12, Supporting Information). Analysis of the excitation dynamics reveals that the 520 nm peak attains its maximum intensity within a few femtoseconds, followed by energy dissipation to other energy bands (Figure 4c). A similar trend was observed for the emission energy levels (Figure 4d). This analysis underscores the rapid transitions and energy redistribution occurring in the system, which are critical for understanding lasing dynamics.

2.5. Chemical Structure Analysis

The chemical structure was also analyzed to elucidate the principles underlying lasing performance. TCQDs underwent post-treatment via secondary solvothermal processing using a mixture of ethanol and ammonia, resulting in a product referred to as oxidized carbon dots (OCDs, Experimental Section). After treatment, the optical properties of OCDs were characterized by steady-state PL and absorption spectra (Figures S13 and S14, Supporting Information). Similar concentration-dependent performances were observed, with the PL spectra covering a range

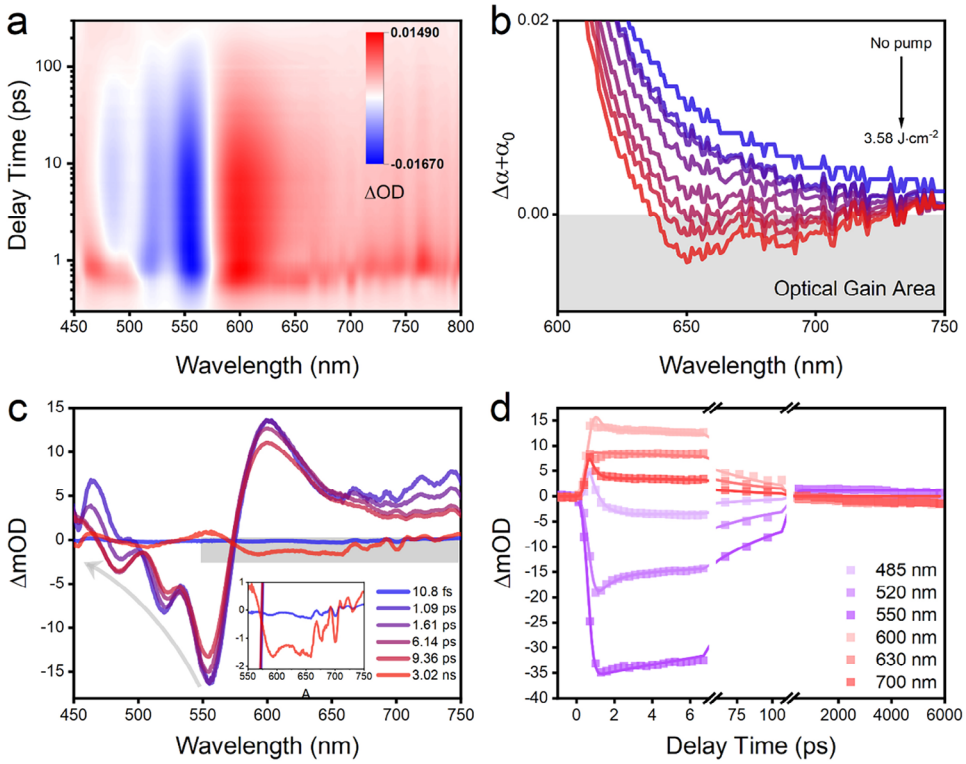

Figure 4. a) Pseudocolour images of TA spectra for the TCQDs (2^{-2} g·L^{-1}) under incident excitation power of 3.58 J•cm^{-2}. b) Optical gain obtained by the TA and steady-state absolute absorption of the TCQDs solutions recorded at a delay time of ≈500 ps. c) TA spectra of TCQDs solution (2^{-2} g·L^{-1}) probed at different time scales. d) TA kinetics of TCQDs solution (2^{-2} g·L^{-1}) probed at different wavelengths.

from 585 to 680 nm (Figure S15, Supporting Information). However, no new absorption or PLE peaks emerged in the spectra, indicating that the FRET effect led to an increase in non-radiative channels, thereby disrupting the process of population inversion (Figure S16, Supporting Information). OCDs could not emit lasing even under ultrahigh energy excitation (Figure S17, Supporting Information).

X-ray photoelectron spectroscopy (XPS) was employed to investigate the elemental composition and chemical structures of both carbon dot variants (Figure S18a–h and Table S1, Supporting Information). The detailed composition of each element is presented in Table S1 (Supporting Information). The percentages of the four elements showed minimal change after secondary solvothermal treatment, except for an increase in the content of C═C and C—C bonds, indicating a higher degree of graphitization, which is a normal phenomenon following high-temperature and high-pressure reactions. Notable changes in elemental analysis were observed in the oxygen- and nitrogen-related compositions.[27,28] After the reaction, N—H functional groups in OCDs disappeared compared to TCQDs, along with the C═O group. These significant differences suggest that functional groups, such as amides and carboxylic acids, attached to the surface of TCQDs were substituted by other active groups. Interestingly, the amino group did not increase despite the introduction of ammonia during the reaction, indicating that ammonia acted solely as a solvent to create an extreme environment rather than as a precursor. Similar results were obtained from Fourier-transform infrared spectroscopy (FT-IR) (Figure S19i,j, Supporting Information), where the stretching vibration of N—H at ≈3250 cm^{-1} was not detected after the reaction.

2.6. Concentration-Dependent Programmable Mode Spacing Laser

Similar tunable mode-spacing trends were observed in the lasing spectra for the three additional concentrations as shown in **Figure 5**. For solutions with 2^{-1} g·L-1 in DMF, the mode spacing could be adjusted from 0.89 to 2.57 nm as the cavity length was reduced. Interestingly, at 2^{-2} g·L^{-1}, two lasing peaks with controllable mode spacing emerged simultaneously in a single PL spectrum. Calculation using the equation $\Delta\lambda = \lambda^2/(2n_{\text{eff}}L)$ showed that the variation range for 655 nm (1.28 nm to 3.33 nm) was narrower than that for 703 nm (1.50 nm to 3.98 nm) as the cavity length changed. At a lower concentration of 2^{-3} g·L^{-1}, a shorter modulable lasing band appeared at 641 nm, with mode spacing ranging from 2.02 to 3.03 nm. All experimental results align with theoretical predictions (Figure S19, Supporting Information). Reducing CQDs concentration decreases scattering losses but elevates the lasing threshold, complicating the suppression of competing modes. Future efforts will focus on designing more precise cavity geometries to achieve single-mode lasing across a wider spectral range.

To validate the broader applicability of the adjustable mode-spacing technique for liquid gain media, we tested two organic dye solutions: Rhodamine B (RhB) and Nile Blue (Figure S20, Supporting Information). At a concentration of 1 g·L^{-1},

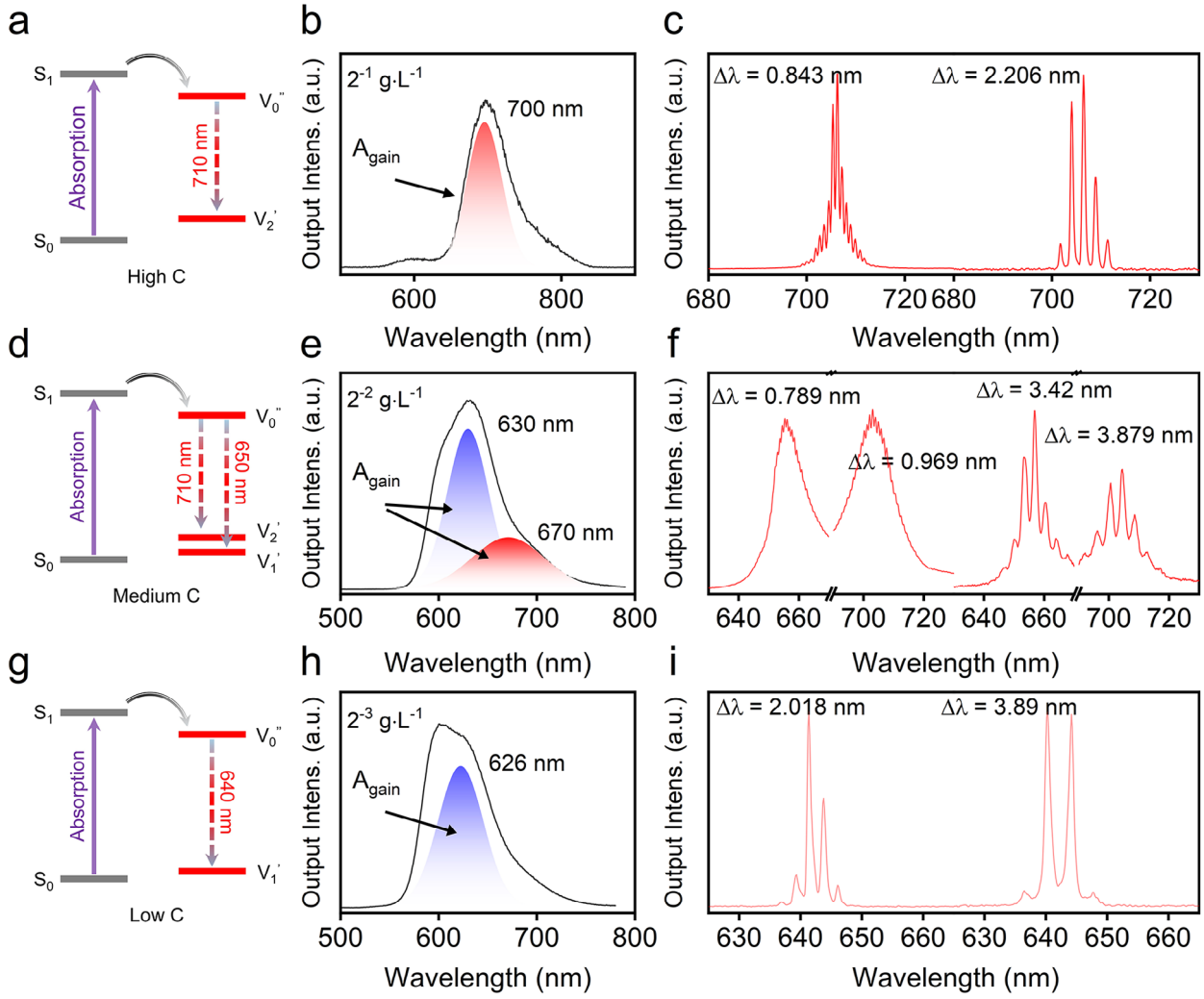

Figure 5. Schematic diagrams of various concentration-dependent lasing transitions at a) 2^{-1} g•L^{-1}. d) 2^{-2} g•L^{-1}. g) 2^{-3} g•L^{-1}. Fitted emission spectra at gradient concentration. b) 2^{-1} g•L^{-1}. e) 2^{-2} g•L^{-1}. h) 2^{-3} g•L^{-1}. All the spectra can be deconvoluted to 3 peaks ≈600, 630, and 700 nm. Lasing spectra of TCQDs solution in DMF with a concentration of c) 2^{-1} g·L^{-1}. f) 2^{-2} g·L^{-1}. i) 2^{-3} g·L^{-1} under the influence of external mirror.

the RhB laser exhibited tunable mode spacing from 0.85 to 2.35 nm with decreasing cavity length, while Nile Blue demonstrated mode spacing ranging from 1.063 to 1.625 nm. All experimental results align closely with theoretical predictions derived from the Fabry-Pérot cavity model (Figure S20d,h, Supporting Information).

3. Conclusion

In summary, we employed a quartz cuvette filled with CQDs dispersed in DFM as the liquid gain medium. The FRET-based multi-level system in CQDs enables population inversion at low energy thresholds and delivers a broad gain bandwidth between 641 and 710 nm. The refractive index matching between the liquid gain medium and the quartz cuvette enables the formation of a gain-guided optical waveguide, producing low-divergence-angle beam emission. This emission facilitates efficient coupling of external optical feedback, as the collimated beam propagation ensures that reflected light from the external mirror retains minimal divergence, thereby enhancing the feedback mechanism's efficiency. By precisely adjusting the external mirror separation, we achieved modal control of the liquid-based CQD laser, enabling transitions from random lasing to multimode Fabry–Pérot lasing and finally single-mode lasing. The strong optical feedback, characterized by its long penetration length, suppresses random modes associated with short closed-loop cavities, stabilizing Fabry–Pérot mode operation. Stable single-mode lasing at 715 nm was achieved through meticulous mirror positioning. This methodology is broadly applicable to colloidal quantum dots as liquid-state gain media, establishing a universal platform for spectrally tunable lasers.

4. Experimental Section

Materials: *O*-phenylenediamine (99.9%), Sulfuric acid (95.0–98.0%), Sodium hydroxide (98%), Anhydrous ethanol (99.9%), Acetone (99.5%), N,N-Dimethylformamide (≥99.8%), Dimethyl sulfoxide (≥s99.8%) were all purchased from Sigma–Aldrich without further purification.

Preparation of Color-Tunable Carbon Quantum Dots (TCQDs): TCQDs were synthesized via a solvothermal approach. Initially, *O*-phenylenediamine (0.6 g) was ultrasonically dissolved in cooled concentrated sulfuric acid (4.6 M, 20 mL) to obtain a transparent solution. This solution was transferred into a 50 mL PTFE autoclave and heated at 200 °C for 12 h. After cooling to room temperature, the crude products were centrifuged at 10 000 rpm for 10 min to eliminate insoluble materials, followed by filtration through 0.22 µm PTFE microporous membranes. The filtrate was subsequently mixed with a rotating solution of sodium hydroxide (1.25 M, 50 mL) and stirred for an additional 60 min, with a sealing membrane used to retain the heat generated by acid-base neutralization. Finally, the products were collected by centrifugation at 10 000 rpm for 10 min, washed 3 to 4 times with a mixture of anhydrous ethanol and water, and dried in an oven at 60 °C to yield TCQDs powder.

Preparation of Oxidized Carbon Dots (OCDs): 20 mg of TCQDs were ultrasonically dispersed in ethanol (20 mL) and subsequently subjected to an additional solvothermal reaction at 200 °C for 12 h. After cooling to room temperature (RT), the crude product was centrifuged to obtain the OCDs powder, followed by washing with a mixed solvent of distilled water and ethanol.

Computer Simulations: The electric field was simulated using finite element method (FEM) from COMSOL Multiphysics software. A wave optics module was selected to build the model, with two ports along the extension direction of the waveguide set to simulate the guided light wave. The frequency of the light wave at the target was input to solve the corresponding electric field distribution. All materials were considered homogeneous and were defined by input refractive indices.

General Material Characterizations: Low- and high-resolution transmission electron microscopy (TEM) measurements were conducted using a JEM-2100F transmission electron microscope (JEOL) operating at an acceleration voltage of 200 kV. UV–vis spectra were acquired using a Shimadzu UV-2550 spectrophotometer. Steady-state fluorescence spectra were measured with an Edinburgh Instruments FLS920 spectrometer equipped with a xenon arc lamp excitation source. Time-resolved photoluminescence (TRPL) measurements were conducted via a time-correlated single-photon counting (TCSPC) system, utilizing a 375 nm picosecond-pulsed laser for excitation. Transient absorption spectroscopy was conducted using 400 nm, 50 fs pulses as the pump source and continuum white-light, 50 fs pulses as the probe source. FT-IR data were acquired using a Bruker Vertex-70 FTIR spectrometer in ATR mode. X-ray photoelectron spectroscopy (XPS) data were obtained using a Nexsa G2 surface analysis system (Thermo Scientific).

Lasing Characterizations: The lasing characteristics of the samples in the cuvette were examined under optical excitation with and without optical feedback using a frequency-quadrupled Q-switched Nd: YAG laser operating in pulsed mode (532 nm, ≈6 ns pulse width, 10 Hz repetition rate). The experimental setup was illustrated in Figure S21 (Supporting Information). A 5 mm-long pump stripe with a thickness of ≤100 µm was projected onto the shorter edge of the cuvette, which was filled with a liquid gain medium, by focusing the 532 nm laser beam through a cylindrical lens [38]. Upon excitation, the generated light was confined in the *y*- and *z*-directions and propagated along the *x*-direction, forming a gain-guided waveguide (see the red line in the liquid shown in Figure 2b). This configuration facilitated light emission through the two surfaces of the cuvette's longer edges in the direction perpendicular to the *x*-axis. To introduce optical feedback along the *x*-direction, an optically flat aluminum mirror was positioned parallel to one of the cuvette's longer edges, while lasing emission was collected from the opposite side. The separation between the mirror and the cuvette was precisely adjusted using a three-axis translation stage.

Optical Gain and Loss Measurement: The optical gain of the carbon dots was measured using the variable stripe length (VSL) method. The photoluminescence intensity, $I(\lambda)$, emitted from the edge of the cuvette was coupled to a spectrum analyzer (SPEC-CMS960). The net optical gain, $G(\lambda)$, was calculated by fitting the equation $I(\lambda) = I_{sp}(\lambda)\ (\exp[G(\lambda)L] - 1)/G(\lambda)$ to measure $I(\lambda)$ values across a range of stripe lengths, L, where λ represents the emission wavelength and $I_{sp}(\lambda)$ was the spontaneous emission intensity. Cavity loss in the carbon dots solution was measured using the variable cavity length (VCL) method. Incident laser light at the emission wavelength of the carbon dots was focused onto the cuvette surface, and the transmitted power was measured using a power meter positioned behind the cuvette. The cavity loss, α_{cav}, was calculated by fitting the equation $ln(T(\lambda)) = -2\alpha_{cav}L$, where T is the transmittance ratio, λ is the emitting wavelength and L corresponds to the optical path length.

Supporting Information

Supporting Information is available from the Wiley Online Library or from the author.

Acknowledgements

X.D. and P.W. contributed equally to this work. This work was supported by Shenzhen Science and Technology Program Basic Research Project (General Program) JCYJ20220531090801004.

Conflict of Interest

The authors declare no conflict of interest.

Data Availability Statement

Research data are not shared.

Keywords

carbon quantum dots, Förster resonance energy transfer, gain-guided waveguide, liquid-state laser, tumable wavelength

Received: March 17, 2025
Revised: June 5, 2025
Published online: June 27, 2025

[1] L. Ai, H. Wang, B. Wang, S. Liu, H. Song, S. Lu, *Adv. Mater.* **2024**, *36*, 2410094.
[2] W. F. Zhang, H. Zhu, S. F. Yu, H. Y. Yang, *Adv. Mater.* **2012**, *24*, 2263.
[3] F. Yuan, Y.-K. Wang, G. Sharma, Y. Dong, X. Zheng, P. Li, A. Johnston, G. Bappi, J. Z. Fan, H. Kung, B. Chen, M. I. Saidaminov, K. Singh, O. Voznyy, O. M. Bakr, Z.-H. Lu, E. H. Sargent, *Nat. Photonics* **2020**, *14*, 171.
[4] G. Hu, Y. Wang, S. Zhang, H. Ding, Z. Zhou, J. Wei, X. Li, H. Xiong, *Carbon* **2023**, *203*, 1.
[5] Z. Xie, F. Wang, C.-y. Liu, *Adv. Mater.* **2012**, *24*, 1716.
[6] B. Wang, Z. Wei, L. Sui, J. Yu, B. Zhang, X. Wang, S. Feng, H. Song, X. Yong, Y. Tian, B. Yang, S. Lu, *Light: Sci. Appl.* **2022**, *11*, 172.
[7] Y. Liu, L. Cao, P. Wang, X. Pang, L. Li, Q. Mei, W.-F. Dong, M. Zan, *Chem. Eng. J.* **2023**, *470*, 144349.
[8] L. Ai, Z. Song, M. Nie, J. Yu, F. Liu, H. Song, B. Zhang, G. I. N. Waterhouse, S. Lu, *Angew. Chem., Int. Ed.* **2023**, *62*, 202217822.
[9] Y. Zhang, J. Wang, L. Wang, R. Fu, L. Sui, H. Song, Y. Hu, S. Lu, *Adv. Mater.* **2023**, *35*, 2302536.
[10] F. Wang, X. Dong, Y. Zuo, Z. Xie, R. Guan, *Mater. Today Phys.* **2024**, *41*, 101332.

[11] J. Wang, S. Zhang, Y. Li, C. Wu, W. Zhang, H. Zhang, Z. Xie, S. Zhou, *Small* **2022**, *18*, 2203152.
[12] S. Qu, X. Liu, X. Guo, M. Chu, L. Zhang, D. Shen, *Adv. Funct. Mater.* **2014**, *24*, 2689.
[13] T. Nagafusa, Y. Hara, K. Nishio, T. Isshiki, K. Yamashita, *Adv. Opt. Mater.* **2022**, *10*, 2200255.
[14] H. Zhu, W. Zhang, S. F. Yu, *Nanoscale* **2013**, *5*, 1797.
[15] F. Yuan, Z. Xi, X. Shi, Y. Li, X. Li, Z. Wang, L. Fan, S. Yang, *Adv. Opt. Mater.* **2019**, *7*, 1801202.
[16] X. Lin, Y. Yang, X. Li, Y. Lv, Z. Wang, J. Du, X. Luo, D. Zhou, C. Xiao, K. Wu, *Nat. Nanotechnol.* **2024**, *20*, 229.
[17] D. Hahm, V. Pinchetti, C. Livache, N. Ahn, J. Noh, X. Li, J. Du, K. Wu, V. I. Klimov, *Nat. Mater.* **2024**, *24*, 48.
[18] S. Prakash, S. Sahu, S. Bhattacharya, P. B. Bisht, A. K. Mishra, *Chem. Asian J.* **2021**, *16*, 783.
[19] A. Madonia, G. Minervini, A. Terracina, A. Pramanik, V. Martorana, A. Sciortino, C. M. Carbonaro, C. Olla, T. Sibillano, C. Giannini, E. Fanizza, M. L. Curri, A. Panniello, F. Messina, M. Striccoli, *ACS Nano* **2023**, *17*, 21274.
[20] B. K. Barman, D. Hernández-Pinilla, O. Cretu, R. Ohta, K. Okano, T. Shiroya, J. Sasai, K. Kimoto, T. Nagao, *ACS Sustainable Chem. Eng.* **2023**, *11*, 12291.
[21] Y. Zhang, H. Song, L. Wang, J. Yu, B. Wang, Y. Hu, S.-Q. Zang, B. Yang, S. Lu, *Angew. Chem., Int. Ed.* **2021**, *60*, 25514.
[22] G. Veronis, Z. Yu, S. E. Kocabas, D. A. B. Miller, M. L. Brongersma, S. Fan, *Opt. Lett.* **2009**, *7*, 302.
[23] J. C. F. Matthews, A. Politi, A. Stefanov, J. L. O'Brien, *Nat. Photonics* **2009**, *3*, 346.
[24] J. Maskoun, N. Gheshlaghi, F. Isik, S. Delikanli, O. Erdem, E. Y. Erdem, H. V. Demir, *Adv. Mater.* **2021**, *33*, 2007131.
[25] L. Cerdán, E. Enciso, V. Martín, J. Bañuelos, I. López-Arbeloa, A. Costela, I. García-Moreno, *Nat. Photonics* **2012**, *6*, 621.
[26] D. Okada, S. Azzini, H. Nishioka, A. Ichimura, H. Tsuji, E. Nakamura, F. Sasaki, C. Genet, T. W. Ebbesen, Y. Yamamoto, *Nano Lett.* **2018**, *18*, 4396.
[27] Y. Zhang, Y. Hu, J. Lin, Y. Fan, Y. Li, Y. Lv, X. Liu, *ACS Appl. Mater. Interfaces* **2016**, *8*, 25454.
[28] H. Ding, S.-B. Yu, J.-S. Wei, H.-M. Xiong, *ACS Nano* **2016**, *10*, 484.